

Optimization with nonstationary, nonlinear monolithic fluid-structure interaction

Thomas Wick¹  | Winnifried Wollner²

¹Institut für Angewandte Mathematik,
Leibniz Universität Hannover, Hannover,
Germany

²Department of Mathematics, Technische
Universität Darmstadt, Darmstadt,
Germany

Correspondence

Thomas Wick, Institut für Angewandte
Mathematik, Leibniz Universität
Hannover, Welfengarten 1, Hannover
30167, Germany.
Email:
thomas.wick@ifam.uni-hannover.de

Summary

Within this work, we consider optimization settings for nonlinear, nonstationary fluid-structure interaction (FSI). The problem is formulated in a monolithic fashion using the arbitrary Lagrangian-Eulerian framework to set-up the fluid-structure forward problem. In the optimization approach, either optimal control or optimal design problems are treated. In the latter, the stiffness of the solid is estimated from given reference values. In the numerical solution, the optimization problem is solved with a gradient-based solution algorithm. The nonlinear subproblems of the FSI forward problem are solved with a Newton method including line search. Specifically, we will formally provide the backward-in-time running adjoint state used for gradient computations. Our algorithmic developments are demonstrated with some numerical examples as, for instance, extensions of the well-known fluid-structure benchmark settings and a flapping membrane test in a channel flow with elastic walls.

KEYWORDS

gradient-based optimization, monolithic formulation, optimal control, optimal design, unsteady nonlinear fluid-structure interaction

1 | INTRODUCTION

This article is devoted to the study of optimal control and optimal design problems of nonstationary, nonlinear fluid-structure interaction (FSI). For general overviews on the FSI forward problem, we refer to the books.¹⁻⁸ FSI is challenging for mainly two reasons. First, the interface must be discretized with sufficient accuracy since otherwise the kinematic and dynamic coupling conditions are not correctly transferred to the other problem. Evidence is given in Reference 4 [p. 415ff] in which the FSI-2 benchmark is not listed (p. 424-425) because most codes were not able to obtain robust results under spatial and temporal refinement. Specifically, the elastic beam will only start moving when the interface conditions are accurately resolved. Second, numerical algorithms are sensitive in terms of stability to the physical parameters; known as added-mass effect.⁹⁻¹² In order to formulate the fluid equations to match with the solid Lagrangian coordinate system at the interface, we employ the well-known arbitrary Lagrangian-Eulerian (ALE) technique.¹³⁻¹⁵ Here, we notice that two schools exist: the ALE formulation of the time derivative, for example, References 2,15 in which the flow problem is still given in the moving domain $\Omega(t)$ and^{16,17} in which the entire flow problem is rewritten in the reference

[Correction added on, after first online publication: Projekt Deal funding statement has been added.]

This is an open access article under the terms of the Creative Commons Attribution License, which permits use, distribution and reproduction in any medium, provided the original work is properly cited.

© 2020 The Authors. *International Journal for Numerical Methods in Engineering* published by John Wiley & Sons Ltd.

domain $\hat{\Omega}$. In this work, we follow the second approach because both authors have made excellent computational and theoretical experiences as indicated in References 18–23. Specifically, these studies include matching of stationary and nonstationary FSI benchmark values (proposed in Reference 1 and detailed comparisons of several groups, including us, are presented in Reference 4), adjoint-based goal-oriented error estimation for spatial and temporal mesh refinements, a parallel monolithic solver substantiated with scalability studies, and well-posedness results as well as differentiability with respect to problem data for stationary FSI.

Employing FSI as forward problem within an optimization framework contains the previously mentioned difficulties and yields significant further challenges when dealing with nonstationary problem settings. Historically, this subject falls into the category of partial differential equation (PDE)-constrained optimization.²⁴ Studies concentrating on theoretical and computational aspects for stationary FSI optimization are.^{23,25–27} Here, we notice that the required adjoints are the same as used for adjoint-based error estimation; see, for instance, References 28, 29. Nonlinear (stationary) FSI investigating various partitioned coupling techniques was recently subject in Reference 30. The by far more challenging situation of nonstationary settings is listed in the following. A nonstationary situation assuming a rigid solid was theoretically studied in Reference 31. Further theoretical results for a boundary control FSI problem were established in Reference 32. Parameter estimation to detect the stiffness of an arterial wall with a well-posedness analysis and numerical simulations was addressed in Reference 33. Again in blood flow simulations, data assimilation problem were formulated in References 34 and ³⁵, in which however, the arterial walls were not considered. A full FSI problem for data assimilation using a Kalman filter was subject in Reference 36 and applied in References 37, 38 to the identification of arterial wall stiffnesses. In Reference 39, the authors used optimization techniques to formulate the FSI coupling conditions. Adjoint for one-dimensional FSI were derived in References 40, 41. Reduced basis methods for FSI-based optimization were developed in Reference 42. Optimal control of nonstationary FSI applied to benchmark settings was investigated in Reference 43. A linearized FSI optimization problem was addressed in Reference 44 and detailed results for full-time-dependent FSI optimal control were summarized in Reference 45. In this respect, we also mention²¹ in which the adjoints required for optimization were employed for dual-weighted residual error estimation for time adaptivity. Most recently, a uncertainty quantification framework for FSI with applications in aortic biomechanics was developed in Reference 46.

The significance of the current work is on the development of a fully monolithic formulation for gradient-based optimization for nonstationary, nonlinear FSI problems. For the gradient computation, we employ the adjoint. One burden in this approach is the derivation, implementation, and computation of the additional adjoint equation. On the other hand, adjoint approaches allow an easy calculation of the gradient, for example, References 47,48, independent of the dimension of the control space. In this context, the formulation of the FSI problem in a reference domain has become popular in optimization as it allows for a convenient variational setting with fixed function spaces independent of the current deformed domain, for example, Reference 49.

For this reason, we are interested in an FSI formulation in a common coordinate system. To this end, the coupled problem is prescribed in the reference configuration with the help of the ALE approach in a variational-monolithic way. As previously summarized in our literature review, only very few results exist to date for such a framework. Indeed the challenges consist of both the nonlinearities and the nonstationary nature of the problem. FSI in the forward state is itself a highly nonlinear problem. Moreover, interesting nonstationary configurations require several thousands of time steps. For instance, the FSI three benchmark^{4,16} requires about 6000 to 10 000 time steps for a fully developed oscillatory solution. These are costly computations, even for a moderate number of spatial degrees of freedom. Numerically, an inf-sup stable spatial discretization is applied to the FSI forward problem. Time discretization is based on a one-step-theta formulation. The discretized subproblems are solved with Newton solver including line search. In order to apply gradient-based techniques, the adjoint state is running backward-in-time and must access the primal solution at the time points when treating nonlinear problems. Such derivations and implementations are very tedious. In this work, we carefully derive and implement them in order to test their performance. Our overall approach is a discretize-then-optimize technique since time discretization is not derived from a Galerkin scheme. The advantage of this approach is that all solution unknowns are discretized first. Consequently, the computation of derivatives is a priori simpler since we work in finite-dimensional spaces and the discretization of the adjoint variable is determined by the test space for the discrete state. These are tested with the help of the modification of well-known FSI benchmark settings^{4,16} and a flapping membranes example that was originally proposed in Reference 50 and later modified in Reference 51.

The outline of this article is as follows: In Section 2, the equations for fluid flow and solids are summarized. Moreover, the FSI setting is formulated in a monolithic fashion using the ALE framework. Section 3 contains temporal and spatial discretizations. The main results are presented in Section 4 in which the gradient computation, including details on the adjoint, are presented. In Section 5 the solution algorithms for the FSI optimization framework are presented. Our

algorithmic techniques are substantiated with several numerical tests in Section 6. We summarize our main findings in Section 7.

2 | MODELING THE FSI FORWARD PROBLEM

2.1 | Notation

We denote by $\Omega := \Omega(t) \subset \mathbb{R}^d$, $d = 2$, the domain of the FSI problem. The domain consists of two time-dependent subdomains $\Omega_f(t)$ and $\Omega_s(t)$. The FSI-interface between $\Omega_f(t)$ and $\Omega_s(t)$ is denoted by $\Gamma_i(t) = \overline{\partial\Omega_f(t)} \cap \overline{\partial\Omega_s(t)}$. The initial (or later reference) domains are denoted by $\hat{\Omega}$, $\hat{\Omega}_f$, and $\hat{\Omega}_s$, respectively, with the interface $\hat{\Gamma}_i = \partial\hat{\Omega} \cap \partial\hat{\Omega}$. Furthermore, we denote the outer boundary by $\partial\hat{\Omega} = \hat{\Gamma} = \hat{\Gamma}_{\text{in}} \cup \hat{\Gamma}_D \cup \hat{\Gamma}_{\text{out}}$ where $\hat{\Gamma}_D$ and $\hat{\Gamma}_{\text{in}}$ are Dirichlet boundaries (for the velocities and displacements) and $\hat{\Gamma}_{\text{out}}$ denotes a fluid outflow Neumann boundary, respectively. The displacements are set to zero on $\hat{\Gamma}_{\text{out}}$.

As frequently used in the literature, we denote the L^2 scalar product in Ω with $(a, b) := (a, b)_\Omega := \int_\Omega a \cdot b \, dx$ for vectors a, b . For (second-order) tensor-valued functions A, B , it yields $(A, B) := (A, B)_\Omega := \int_\Omega A : B \, dx$, where $A : B = \sum_{ij=1}^d A_{ij}B_{ij}$ and A_{ij} and B_{ij} are the entries of A and B .

2.2 | Spaces

For the function spaces in the (fixed) reference domains $\hat{\Omega}$, $\hat{\Omega}_f$, $\hat{\Omega}_s$, we define spaces for spatial discretization only. Rather than employing Bochner-spaces^{52,53} for space-time functions, the time t is later explicitly accounted for, for example, Reference 54 (Section 7.1). Here, let $I := [0, T]$ be the time interval and T the end time value. First, we define

$$\hat{V} := H^1(\hat{\Omega})^d.$$

Next, in the fluid domain, we define further:

$$\begin{aligned} \hat{L}_f &:= L^2(\hat{\Omega}_f), \\ \hat{L}_f^0 &:= L^2(\hat{\Omega}_f)/\mathbb{R}, \\ \hat{V}_f^0 &:= \{\hat{v}_f \in H^1(\hat{\Omega}_f)^d : \hat{v}_f = 0 \text{ on } \hat{\Gamma}_{\text{in}} \cup \hat{\Gamma}_D\}, \\ \hat{V}_{f,\hat{u}}^0 &:= \{\hat{u}_f \in H^1(\hat{\Omega}_f)^d : \hat{u}_f = \hat{u}_s \text{ on } \hat{\Gamma}_i, \hat{u}_f = 0 \text{ on } \hat{\Gamma}_{\text{in}} \cup \hat{\Gamma}_D \cup \hat{\Gamma}_{\text{out}}\}, \\ \hat{V}_{f,\hat{u},\hat{\Gamma}_i}^0 &:= \{\hat{\psi}_f \in H^1(\hat{\Omega}_f)^d : \hat{\psi}_f = 0 \text{ on } \hat{\Gamma}_i \cup \hat{\Gamma}_{\text{in}} \cup \hat{\Gamma}_D \cup \hat{\Gamma}_{\text{out}}\}. \end{aligned}$$

In the solid domain, we use

$$\begin{aligned} \hat{L}_s &:= L^2(\hat{\Omega}_s)^d, \\ \hat{V}_s^0 &:= \{\hat{u}_s \in H^1(\hat{\Omega}_s)^d : \hat{u}_s = 0 \text{ on } \hat{\Gamma}_D\}. \end{aligned}$$

For the FSI problem using variational-monolithic coupling^{17,55,56} the velocity spaces are extended from $\hat{\Omega}_f$ and $\hat{\Omega}_s$ to the entire domain $\hat{\Omega}$ such that we can work with global H^1 functions. Thus, we define:

$$\hat{V}^0 := \{\hat{v} \in H^1(\hat{\Omega})^d : \hat{v} = 0 \text{ on } \hat{\Gamma}_{\text{in}} \cup \hat{\Gamma}_D\}. \quad (1)$$

By this choice, the kinematic and dynamic coupling conditions are automatically satisfied in a variational sense.

Finally, we notice that the spaces on the current domains Ω , Ω_f , Ω_s are defined correspondingly without “hat” notation.

2.3 | The ALE concept, transformed fluid flow, and solids in Lagrangian coordinates

In this section, we recapitulate the ingredients to formulate a coupled problem (ie, FSI) with the help of the ALE approach. The ALE mapping $\hat{\mathcal{A}} : \hat{\Omega}_f \rightarrow \Omega_f$ is defined first.

2.3.1 | The ALE transformation and ALE time-derivative

First, we define the ALE transformation:

Definition 1. The ALE mapping is defined in terms of the vector-valued (artificial) fluid mesh displacement $\hat{u}_f : \hat{\Omega}_f \rightarrow \mathbb{R}^d$ such that

$$\hat{\mathcal{A}}(\hat{x}, t) : \hat{\Omega}_f \times I \rightarrow \Omega_f, \quad \text{with } \hat{\mathcal{A}}(\hat{x}, t) = \hat{x} + \hat{u}_f(\hat{x}, t), \quad (2)$$

which is specified through the deformation gradient and its determinant

$$\hat{F} := \hat{\nabla} \hat{\mathcal{A}} = \hat{I} + \hat{\nabla} \hat{u}_f, \quad \hat{J} := \det(\hat{F}). \quad (3)$$

Furthermore, function values in Eulerian and Lagrangian coordinates are identified by

$$u_f(x) =: \hat{u}_f(\hat{x}), \quad \text{with } x = \hat{\mathcal{A}}(\hat{x}, t). \quad (4)$$

Here, \hat{I} denotes the identity matrix. The mesh velocity is defined by $\hat{w} := \partial_t \hat{\mathcal{A}}$. The key quantity to measure the fluid mesh regularity is \hat{J} . The artificial fluid displacement \hat{u}_f (the mesh motion) is obtained in this work by solving a biharmonic equation.^{19,26,56,57}

Finally, the transformation between different coordinate systems requires transformation of derivatives. For a vector-valued function $u \in \Omega$ and $\hat{u} \in \hat{\Omega}$ it holds, for example, Reference 58:

$$\nabla u = \hat{\nabla} \hat{u} \hat{F}^{-1}.$$

Finally, the ALE time-derivative is the total derivative of an Eulerian field and is important when working on moving domains:

$$\partial_t|_{\hat{\mathcal{A}}} v_f(x, t) = \hat{w} \cdot \nabla v_f + \partial_t v_f(x, t). \quad (5)$$

2.4 | Equations for fluids and solids

In this section, we briefly state the basic underlying equations first separately. In the following, we first present fluid flow and then the solid part.

2.4.1 | Strong forms

The isothermal, incompressible Navier-Stokes equations in an ALE setting read: Given v_{in}, h_f , and v_0 ; find $v_f : \Omega_f(t) \times I \rightarrow \mathbb{R}^d$ and $p_f : \Omega_f(t) \times I \rightarrow \mathbb{R}$ such that

$$\begin{aligned} \rho_f \partial_t|_{\hat{\mathcal{A}}} v_f + \rho_f (v_f - \hat{w}) \cdot \nabla v_f - \nabla \cdot \sigma_f(v_f, p_f) &= 0, \quad \nabla \cdot v_f = 0 \quad \text{in } \Omega_f(t), \\ v_f^D &= v_{\text{in}} \quad \text{on } \Gamma_{\text{in}}, \quad v_f = 0 \quad \text{on } \Gamma_D, \quad -p_f n_f + \rho_f v_f \nabla v_f \cdot n_f = 0 \quad \text{on } \Gamma_{\text{out}}, \quad v_f = h_f \quad \text{on } \Gamma_i, \\ v_f(0) &= v_0 \quad \text{in } \Omega_f(0), \end{aligned}$$

where the (symmetric) Cauchy stress is given by

$$\sigma_f(v_f, p_f) := -pI + \rho_f v_f (\nabla v + \nabla v^T),$$

with the density ρ_f and the kinematic viscosity ν_f . Later in the FSI problem, the function h_f will be given by the solid velocity v_s . The normal vector is denoted by n_f .

The equations for geometrically nonlinear elastodynamics are given as follows: Given \hat{h}_s, \hat{u}_0 , and \hat{v}_0 ; find $\hat{u}_s : \hat{\Omega}_s \times I \rightarrow \mathbb{R}^d$ such that

$$\begin{aligned} \hat{\rho}_s \partial_t^2 \hat{u}_s - \hat{\nabla} \cdot (\hat{F} \hat{\Sigma}) &= 0 \quad \text{in } \hat{\Omega}_s, \\ \hat{u}_s &= 0 \quad \text{on } \hat{\Gamma}_D, \quad \hat{F} \hat{\Sigma} \cdot \hat{n}_s = \hat{h}_s \quad \text{on } \hat{\Gamma}_i, \\ \hat{u}_s(0) &= \hat{u}_0 \quad \text{in } \hat{\Omega}_s \times \{0\}, \quad \hat{v}_s(0) = \hat{v}_0 \quad \text{in } \hat{\Omega}_s \times \{0\}. \end{aligned}$$

The constitutive law is given by the tensor:

$$\hat{\Sigma} = \hat{\Sigma}_s(\hat{u}_s) = 2\mu \hat{E} + \lambda \text{tr}(\hat{E})I, \quad \text{with } \hat{E} = \frac{1}{2}(\hat{F}^T \hat{F} - I). \quad (6)$$

Here, μ and λ are the Lamé coefficients for the solid. The solid density is denoted by $\hat{\rho}_s$ and the solid deformation gradient is $\hat{F} = \hat{I} + \hat{\nabla} \hat{u}_s$. Later in FSI, the vector-valued function \hat{h}_s will be given by the normal stress from the fluid problem. Furthermore, \hat{n}_s denotes the normal vector.

2.4.2 | Variational forms

The previous Navier-Stokes equations in a variational ALE framework described in a reference domain $\hat{\Omega}_f$ are given by:

Formulation 1 (ALE Navier-Stokes in $\hat{\Omega}_f$). Let \hat{v}_f^D a suitable extension of Dirichlet inflow data. Find vector-valued velocities and a scalar-valued pressure $\{\hat{v}_f, \hat{p}_f\} \in \{\hat{V}_f^D + \hat{V}_f^0\} \times \hat{L}_f^0$ such that the initial data $\hat{v}_f(0) = \hat{v}_f^0$ are satisfied, and for almost all times $t \in I$ holds:

$$\begin{aligned} \hat{\rho}_f (\hat{J} \partial_t \hat{v}_f, \hat{\psi}_f^v)_{\hat{\Omega}_f} + \hat{\rho}_f (\hat{J} \hat{F}^{-1} (\hat{v}_f - \hat{w}) \cdot \hat{\nabla} \hat{v}_f, \hat{\psi}_f^v)_{\hat{\Omega}_f} + (\hat{J} \hat{\sigma}_f \hat{F}^{-T}, \hat{\nabla} \hat{\psi}_f^v)_{\hat{\Omega}_f} \\ - (\hat{J} \hat{g}_f \hat{F}^{-T} \hat{n}_f, \hat{\psi}_f^v)_{\hat{\Gamma}_{\text{out}}} - (\hat{J} \hat{\sigma}_f \hat{F}^{-T} \hat{n}_f, \hat{\psi}_f^v)_{\hat{\Gamma}_i} = 0 \quad \forall \hat{\psi}_f^v \in \hat{V}_f^0, \\ (\text{div} (\hat{J} \hat{F}^{-1} \hat{v}_f), \hat{\psi}_f^p)_{\hat{\Omega}_f} = 0 \quad \forall \hat{\psi}_f^p \in \hat{L}_f^0. \end{aligned}$$

Here, $\hat{g}_f := -\hat{\rho}_f \nu_f \hat{F}^{-T} \hat{\nabla} \hat{v}_f^T$ denotes a correction term on the outflow boundary and \hat{n}_f is the outer normal vector. The transformed Cauchy stress tensor reads:

$$\hat{\sigma}_f = -\hat{p}_f \hat{I} + 2\hat{\rho}_f \nu_f (\hat{\nabla} \hat{v}_f \hat{F}^{-1} + \hat{F}^{-T} \hat{\nabla} \hat{v}_f^T). \quad (7)$$

The variational formulation for elastodynamics can be formulated as a first-order-in-time system:

Formulation 2. (First-order system in time weak formulation of elasticity including strong damping). Find $\hat{u}_s \in \hat{V}_s^0$ and $\hat{v}_s \in \hat{L}_s$ with the initial data $\hat{u}_s(0) = \hat{u}_0$ and $\hat{v}_s(0) = \hat{v}_0$ such that for almost all times $t \in I$:

$$\begin{aligned} \hat{\rho}_s (\partial_t \hat{u}_s, \hat{\psi}_s^v)_{\hat{\Omega}_s} + (\hat{F} \hat{\Sigma}, \hat{\nabla} \hat{\psi}_s^v)_{\hat{\Omega}_s} - (\hat{F} \hat{\Sigma} \hat{n}_s, \hat{\psi}_s^v)_{\hat{\Gamma}_i} = 0 \quad \forall \hat{\psi}_s^v \in \hat{V}_s^0, \\ \hat{\rho}_s (\partial_t \hat{u}_s - \hat{v}_s, \hat{\psi}_s^u)_{\hat{\Omega}_s} = 0 \quad \forall \hat{\psi}_s^u \in \hat{L}_s. \end{aligned}$$

2.5 | Variational-monolithic ALE FSI

2.5.1 | FSI interface coupling conditions

The coupling of a fluid with a solid must satisfy two physical conditions; namely, continuity of velocities and continuity of normal stresses. A third condition of geometric nature is necessary when working with the ALE framework: continuity of displacements, which couples the physical solid \hat{u}_s and the fluid mesh motion \hat{u}_f . Mathematically, the first and third conditions can be classified as (nonhomogeneous) Dirichlet conditions and the second condition is a (nonhomogeneous) Neumann condition.

In variational-monolithic coupling these Dirichlet conditions are built into the corresponding function space by employing a globalized Sobolev space \hat{V}^0 (see (1)). Neumann type conditions are weakly incorporated through interface integrals, which actually cancel out in the later models because of their weak continuity thanks to working with the space \hat{V}^0 .

For the fluid problem, continuity of velocities is required (ie, a kinematic coupling condition):

$$\hat{v}_f = \hat{v}_s \quad \text{on } \hat{\Gamma}_i. \quad (8)$$

To complete the solid problem, we must enforce the balance of the normal stresses on the interface (ie, a dynamic coupling condition):

$$\hat{J}\hat{\sigma}_f\hat{F}^{-T}\hat{n}_f + \hat{F}\hat{\Sigma}\hat{n}_s = 0 \quad \text{on } \hat{\Gamma}_i. \quad (9)$$

For the geometric problem, we have

$$\hat{u}_f = \hat{u}_s \quad \text{on } \hat{\Gamma}_i, \quad (10)$$

from which we obtain immediately $\partial_t \hat{u}_s = \hat{v}_s = \hat{v}_f$ on $\hat{\Gamma}_i$ by temporal differentiation.

2.5.2 | The FSI model using biharmonic mesh motion

Combining the previous equations for fluids and solids and applying biharmonic mesh motion for realizing the ALE mapping, we obtain the following FSI model:^{19,26,56}

Formulation 3. (Variational-monolithic ALE FSI in $\hat{\Omega}$). Let the constitutive laws from before be given and $\hat{\alpha} > 0$ be a small parameter. Find a global vector-valued velocity, vector-valued displacements, additional displacements (due to the splitting of the biharmonic mesh motion model into two second-order equations) and a scalar-valued fluid pressure, that is, $\{\hat{v}, \hat{u}_f, \hat{u}_s, \hat{w}, \hat{p}_f\} \in \{\hat{v}^D + \hat{V}^0\} \times \{\hat{u}_f^D + \hat{V}_{f,\hat{u}}^0\} \times \{\hat{u}_s^D + \hat{V}_s^0\} \times \hat{V} \times \hat{L}_f^0$, such that $\hat{v}(0) = \hat{v}^0$, $\hat{u}_f(0) = \hat{u}_f^0$, and $\hat{u}_s(0) = \hat{u}_s^0$ are satisfied, and for almost all times $t \in I$ holds:

$$\begin{aligned} \text{Fluid/solid momentum} & \left\{ \begin{aligned} & (\hat{J}\hat{\rho}_f\partial_t\hat{v}, \hat{\psi}^v)_{\hat{\Omega}_f} + (\hat{\rho}_f\hat{J}(\hat{F}^{-1}(\hat{v} - \hat{w}) \cdot \hat{\nabla})\hat{v}), \hat{\psi}^v)_{\hat{\Omega}_f} + (\hat{J}\hat{\sigma}_f\hat{F}^{-T}, \hat{\nabla}\hat{\psi}^v)_{\hat{\Omega}_f} \\ & + \langle \hat{\rho}_f\hat{v}_f\hat{J}(\hat{F}^{-T}\hat{\nabla}\hat{v}^T\hat{n}_f)\hat{F}^{-T}, \hat{\psi}^v \rangle_{\hat{\Gamma}_{\text{out}}} \\ & + (\hat{\rho}_s\partial_t\hat{v}, \hat{\psi}^v)_{\hat{\Omega}_s} + (\hat{F}\hat{\Sigma}, \hat{\nabla}\hat{\psi}^v)_{\hat{\Omega}_s} = 0 \quad \forall \hat{\psi}^v \in \hat{V}^0, \end{aligned} \right. \\ \text{Fluid mesh motion (biharmonic/split)} & \left\{ \begin{aligned} & (\hat{\alpha}\hat{\nabla}\hat{w}|_{\hat{\Omega}_f}, \hat{\nabla}\hat{\psi}^u)_{\hat{\Omega}_f} = 0 \quad \forall \hat{\psi}^u \in \hat{V}_{f,\hat{u},\hat{\Gamma}_i}^0, \\ & (\hat{\alpha}\hat{w}, \hat{\psi}^w)_{\hat{\Omega}} - (\hat{\alpha}\hat{\nabla}\hat{u}_{f,s}, \hat{\nabla}\hat{\psi}^w)_{\hat{\Omega}} = 0 \quad \forall \hat{\psi}^w \in \hat{V} \end{aligned} \right. \\ \text{Solid momentum, second equation} & \left\{ \hat{\rho}_s(\partial_t\hat{u}_s - \hat{v}|_{\hat{\Omega}_s}, \hat{\psi}_s^u)_{\hat{\Omega}_s} = 0 \quad \forall \hat{\psi}_s^u \in \hat{L}_s, \right. \\ \text{Fluid mass conservation} & \left\{ (\hat{\text{div}}(\hat{J}\hat{F}^{-1}\hat{v}), \hat{\psi}_f^p)_{\hat{\Omega}_f} = 0 \quad \forall \hat{\psi}_f^p \in \hat{L}_f^0. \right. \end{aligned}$$

The Neumann coupling conditions on $\hat{\Gamma}_i$ are fulfilled in a variational way and cancel in monolithic modeling due to the global test space \hat{V}^0 in which the test functions from both the fluid and the solid subdomains coincide on the interface. Thus, the condition

$$\langle \hat{J}\hat{\sigma}_f\hat{F}^{-T}\hat{n}_f, \hat{\psi}^v \rangle_{\hat{\Gamma}_i} + \langle \hat{F}\hat{\Sigma}\hat{n}_s, \hat{\psi}^v \rangle_{\hat{\Gamma}_i} = 0 \quad \forall \hat{\psi}^v \in \hat{V}^0 \quad (11)$$

is implicitly contained in the above system.

3 | DISCRETIZATION

In this section, we discuss temporal and spatial discretization of the forward problem. Our derivation contains many details on all terms of the FSI forward problem. The overall problem can be posed, however, in an abstract fashion, which facilitates the derivation of the backward-in-time adjoint problem in Section 4.

3.1 | Temporal discretization

Our goal is to apply A-stable finite differences in time. Specifically, time discretization is based on a One-step- θ scheme as presented for the pure FSI problem, Formulation 3, in Reference 19.

In more detail, semidiscretization in time yields a sequence of generalized steady-state problems that are completed by appropriate boundary values at every time step. Let

$$I = \{0\} \cup I_1 \cup \dots \cup I_N$$

be a partition of the time interval I into half open subintervals $I_n := (t_{n-1}, t_n]$ of (time step) size $k := k_n := t_n - t_{n-1}$ with

$$0 = t_0 < \dots < t_N = T.$$

Time derivatives are discretized with a backward difference quotient such that

$$\partial_t \hat{u} \approx \frac{\hat{u} - \hat{u}^{n-1}}{k}, \quad \partial_t \hat{v} \approx \frac{\hat{v} - \hat{v}^{n-1}}{k},$$

where $\hat{u} := \hat{u}^n := \hat{u}(t_n)$, $\hat{v} := \hat{v}^n := \hat{v}(t_n)$, $\hat{u}^{n-1} := \hat{u}(t_{n-1})$, $\hat{v}^{n-1} := \hat{v}(t_{n-1})$. Furthermore, the mesh velocity $\partial_t \hat{\mathcal{A}} = \hat{w}$ is numerically realized as $\hat{w} = k^{-1}(\hat{u}_f - \hat{u}_f^{n-1})$.

Formulation 4. (The time-discretized abstract problem). We aim to find $\hat{U}^n = \{\hat{v}^n, \hat{u}_f^n, \hat{u}_s^n, \hat{w}^n, \hat{p}_f^n\} \in \hat{X}_D^0$, where $\hat{X}_D^0 := \{\hat{v}^D + \hat{V}^0\} \times \{\hat{u}_f^D + \hat{V}_{f,\hat{u}}^0\} \times \hat{V}_s^0 \times \hat{V} \times \hat{L}_f^0$ and $\hat{X} = \hat{V}^0 \times \hat{V}_{f,\hat{u},\hat{\Gamma}_i}^0 \times \hat{V}_s^0 \times \hat{V} \times \hat{L}_f^0$, for all $n = 1, 2, \dots, N$ such that

$$\hat{A}(\hat{U}^n)(\hat{\Psi}) = 0 \quad \forall \hat{\Psi} \in \hat{X}, \quad (12)$$

where the semilinear form $\hat{A}(\cdot)(\cdot)$ is split into

$$\hat{A}(\hat{U}^n)(\hat{\Psi}) := \hat{A}_T(\hat{U}^n)(\hat{\Psi}) + \hat{A}_I(\hat{U}^n)(\hat{\Psi}) + \hat{A}_E(\hat{U}^n)(\hat{\Psi}) + \hat{A}_P(\hat{U}^n)(\hat{\Psi}).$$

Details of this decomposition are provided in Definition 2.

Definition 2 (Arranging the semilinear form $\hat{A}(\hat{U}^n)(\hat{\Psi})$ into groups). We formally split the semilinear form into four categories: time equation terms (including the time derivatives); implicit terms (such as the fluid incompressibility and also the biharmonic mesh motion); pressure terms; and finally all “standard” terms (eg, stress terms, fluid convection). We then obtain the decomposition:

$$\begin{aligned} \hat{A}_T(\hat{U})(\hat{\Psi}) &= (\hat{J} \hat{\rho}_f \partial_t \hat{v}, \hat{\psi}^v)_{\hat{\Omega}_f} - (\hat{\rho}_f \hat{J}(\hat{F}^{-1} \hat{w} \cdot \hat{\nabla}) \hat{v}, \hat{\psi}^v)_{\hat{\Omega}_f} + (\hat{\rho}_s \partial_t \hat{v}, \hat{\psi}^v)_{\hat{\Omega}_s} + (\hat{\rho}_s \partial_t \hat{u}_s, \hat{\psi}_s^u)_{\hat{\Omega}_s}, \\ \hat{A}_I(\hat{U})(\hat{\Psi}) &= (\hat{\alpha} \hat{\nabla} \hat{w}|_{\hat{\Omega}_f}, \hat{\nabla} \hat{\psi}^u)_{\hat{\Omega}_f} + (\hat{\alpha} \hat{w}, \hat{\psi}^w)_{\hat{\Omega}} - (\hat{\alpha} \hat{\nabla} \hat{u}_{f,s}, \hat{\nabla} \hat{\psi}^w)_{\hat{\Omega}} + (\text{div}(\hat{J} \hat{F}^{-1} \hat{v}), \hat{\psi}_f^p)_{\hat{\Omega}_f}, \\ \hat{A}_P(\hat{U})(\hat{\Psi}) &= (\hat{J} \hat{\sigma}_{f,p} \hat{F}^{-T}, \hat{\nabla} \hat{\psi}^v)_{\hat{\Omega}_f}, \\ \hat{A}_E(\hat{U})(\hat{\Psi}) &= (\hat{\rho}_f \hat{J}(\hat{F}^{-1} \hat{v} \cdot \hat{\nabla}) \hat{v}, \hat{\psi}^v)_{\hat{\Omega}_f} + (\hat{J} \hat{\sigma}_{f,vu} \hat{F}^{-T}, \hat{\nabla} \hat{\psi}^v)_{\hat{\Omega}_f} \\ &\quad + \langle \rho_f \hat{J}(\hat{F}^{-T} \hat{\nabla} \hat{v}_f^T) \hat{F}^{-T} \hat{n}, \hat{\psi}^v \rangle_{\hat{\Gamma}_{\text{out}}} + (\hat{F} \hat{\Sigma}, \hat{\nabla} \hat{\psi}^v)_{\hat{\Omega}_s} - (\hat{\rho}_s \hat{v}, \hat{\psi}_s^u)_{\hat{\Omega}_s}, \end{aligned} \quad (13)$$

where the fluid stress tensor $\hat{\sigma}_f$ is further split into $\hat{\sigma}_{f,vu}$, $\hat{\sigma}_{f,p}$:

$$\hat{\sigma}_{f,p} = -\hat{p}_f \hat{I}, \quad \hat{\sigma}_{f,vu} = \rho_f \nu_f (\hat{\nabla} \hat{v} \hat{F}^{-1} + \hat{F}^{-T} \hat{\nabla} \hat{v}^T).$$

The (nonlinear) time derivative in $\hat{A}_T(\hat{U})(\hat{\Psi})$ is approximated by a backward difference quotient. For the time step $t_n \in I$, for $n = 1, 2, \dots, N$ ($N \in \mathbb{N}$), we compute $\hat{v} := \hat{v}^n$, $\hat{u}_i := \hat{u}_i^n$ ($i = f, s$) via

$$\begin{aligned} \hat{A}_T(\hat{U}^n)(\hat{\Psi}) &\approx \frac{1}{k} (\hat{\rho}_f \hat{J}^{n,\theta} (\hat{v} - \hat{v}^{n-1}), \hat{\Psi}^v)_{\hat{\Omega}_f} - \frac{1}{k} (\hat{\rho}_f (\hat{J} \hat{F}^{-1} (\hat{u}_f - \hat{u}_f^{n-1}) \cdot \hat{\nabla}) \hat{v}, \hat{\Psi}^v)_{\hat{\Omega}_f} \\ &\quad + \frac{1}{k} (\hat{\rho}_s (\hat{v} - \hat{v}^{n-1}), \hat{\Psi}^v)_{\hat{\Omega}_s} + \frac{1}{k} (\hat{\rho}_s (\hat{u}_s - \hat{u}_s^{n-1}), \hat{\Psi}^u)_{\hat{\Omega}_s} \\ &=: \frac{1}{k} \hat{A}_{T,k}(\hat{U}^n, \hat{U}^{n-1,t}, \hat{\Psi}), \end{aligned}$$

where we introduce the parameter $\theta \in [0, 1]$. Furthermore, we use

$$\hat{J}^{n,\theta} = \theta \hat{J}^n + (1 - \theta) \hat{J}^{n-1},$$

and $\hat{u}_i^n := \hat{u}_i(t_n)$, $\hat{v}^n := \hat{v}(t_n)$, and $\hat{J} := \hat{J}^n := \hat{J}(t_n)$. In our computations in Section 6, we always consider $\hat{J}^{n,0.5}$. The former time step is given by \hat{v}^{n-1} , and so on for $i = f, s$.

Formulation 5. Let the previous time step solution $\hat{U}^{n-1} = \{\hat{v}^{n-1}, \hat{u}_f^{n-1}, \hat{u}_s^{n-1}, \hat{w}^{n-1}, \hat{p}_f^{n-1}\}$ and the time step $k := k_n = t_n - t_{n-1}$ be given. In order to solve (12), we seek $\hat{U}^n = \{\hat{v}^n, \hat{u}_f^n, \hat{u}_s^n, \hat{w}^n, \hat{p}_f^n\} \in \hat{X}^0$ by employing one-step- θ splitting:

$$\hat{A}_{T,k}(\hat{U}^n, \hat{U}^{n-1})(\hat{\Psi}) + \theta k \hat{A}_E(\hat{U}^n)(\hat{\Psi}) + k \hat{A}_P(\hat{U}^n)(\hat{\Psi}) + k \hat{A}_I(\hat{U}^n)(\hat{\Psi}) = - (1 - \theta) k \hat{A}_E(\hat{U}^{n-1})(\hat{\Psi}). \quad (14)$$

The concrete scheme depends on the choice of the parameter $\theta \in [0, 1]$. For $\theta = 1$ we obtain the strongly A-stable backward Euler scheme (BE). If $k < 0.5$, for $\theta = 0.5 + k$, we obtain the second order (shown for linear parabolic problems in References 59,60), A-stable, globally stabilized, Crank-Nicolson scheme.

Remark 1. Formulation 5 is still nonlinear and continuous on the spatial level.

3.2 | Spatial discretization

The time-discretized formulation is the starting point for the Galerkin discretization in space. To this end, we construct a finite-dimensional subspace $\hat{X}_h^0 \subset \hat{X}^0$ to find an approximate solution to the continuous problem. As previously explained, in the context of our variational-monolithic formulation, the computations are done on the reference configuration $\hat{\Omega}$. We use two-dimensional (2D) shape-regular meshes. A mesh consists of quadrilateral cells \hat{K} . They perform a nonoverlapping cover of the computation domain $\hat{\Omega} \subset \mathbb{R}^d$, $d = 2$. The corresponding mesh is given by $\hat{\mathcal{T}}_h = \{\hat{K}\}$. The discretization parameter in the reference configuration is denoted by \hat{h} and is a cell-wise constant that is given by the diameter $\hat{h}_{\hat{K}}$ of the cell \hat{K} .

On $\hat{\mathcal{T}}_h$, the conforming finite element space for $\{\hat{v}_h, \hat{u}_{f,h}, \hat{u}_{s,h}, \hat{p}_{f,h}, \hat{w}_h\}$ is denoted by the space $\hat{X}_h \subset \hat{X}$. For Navier-Stokes flow, that is, $\{\hat{v}_h, \hat{p}_{f,h}\}$, we prefer the biquadratic, discontinuous-linear Q_2^c/P_1^{dc} element. For the specific definitions of the single elements, we refer the reader to Reference 61. The property of the Q_2^c/P_1^{dc} element is continuity of the velocity values across different mesh cells.⁶² However, the pressure is defined by discontinuous test functions. Therefore, this element preserves local mass conservation, is of low order, gains the *inf-sup stability*, and is an optimal choice for both fluid problems and FSI problems. The two displacement variables, namely, \hat{u}_h, \hat{w}_h are discretized with Q_2^c elements.

In total, the discretized forward problem consists of

Formulation 6. (Abstract forward problem). Given $\hat{U}^0 \in \hat{X}$ finding $\hat{U} = (\hat{U}_h^n)_{n=1}^N \in \hat{X}_h^N$ solving

$$\sum_{n=1}^N \left(\hat{A}_{T,k}(\hat{U}_h^n, \hat{U}_h^{n-1})(\hat{\Psi}_h^n) + \theta k \hat{A}_E(\hat{U}_h^n)(\hat{\Psi}_h^n) + k \hat{A}_P(\hat{U}_h^n)(\hat{\Psi}_h^n) + k \hat{A}_I(\hat{U}_h^n)(\hat{\Psi}_h^n) + (1 - \theta) k \hat{A}_E(\hat{U}_h^{n-1})(\hat{\Psi}_h^n) \right) = 0 \quad \forall (\hat{\Psi}_h^n)_{n=1}^N \in \hat{X}_h^N. \quad (15)$$

This abstract formulation serves as basis to derive the adjoint state in Section 4.

4 | GRADIENT COMPUTATION

We are interested optimal control and the design of material parameters, for example, μ in (6). To this end, we denote by $q \in \mathbb{R}^p$, with $p \geq 1$, the collection of these parameters, and will define suitable cost functionals $\mathcal{J}(q, \hat{U})$ to be minimized. To highlight the dependence of the equation on the parameters q , we add an additional q argument to the form \hat{A} , for example, we consider $\hat{A}_E(q, \hat{U}_h^n)(\hat{\Psi}_h^n)$ instead of $\hat{A}_E(\hat{U}_h^n)(\hat{\Psi}_h^n)$ in (15).

Formulation 7. (Abstract optimization problem). Minimize the cost functional $\mathcal{J}(q, \hat{U}_h^n)$ subject to the state equation $\hat{A}(q, \hat{U}_h^n)(\hat{\Psi}_h^n) = 0$ (defined in Formulation (15)) for $(q, \hat{U}_h^n) \in \mathbb{R}^p \times \hat{X}_h^N$.

Assuming that (15) admits a unique solution for any given q , we can obtain an optimality system by the standard Lagrange formalism, see, for example, References 24,63,64. For a rigorous proof of the required differentiability properties, some progress has been made for stationary FSI-problems in Reference 23. A rigorous derivation of the corresponding adjoints in the context of shape optimization can be found in Reference 65.

The formal Lagrange approach provides an adjoint equation to (15) as

Formulation 8. (Abstract adjoint problem). Find $\hat{Z} \in \hat{X}_h^N$ solving

$$\begin{aligned} & \sum_{n=1}^N \left(\partial_{\hat{U}_h^n} \hat{A}_{T,k}(\hat{U}_h^n, \hat{U}_h^{n-1})(\hat{\Psi}_h^n, \hat{Z}_h^n) + \partial_{\hat{U}_h^{n-1}} \hat{A}_{T,k}(\hat{U}_h^n, \hat{U}_h^{n-1})(\hat{\Psi}_h^{n-1}, \hat{Z}_h^n) \right. \\ & + \theta k \partial_{\hat{U}_h^n} \hat{A}_E(q, \hat{U}_h^n)(\hat{\Psi}_h^n, \hat{Z}_h^n) + k \partial_{\hat{U}_h^n} \hat{A}_P(\hat{U}_h^n)(\hat{\Psi}_h^n, \hat{Z}_h^n) + k \partial_{\hat{U}_h^n} \hat{A}_I(\hat{U}_h^n)(\hat{\Psi}_h^n, \hat{Z}_h^n) \\ & \left. + (1 - \theta) k \partial_{\hat{U}_h^{n-1}} \hat{A}_E(q, \hat{U}_h^{n-1})(\hat{\Psi}_h^{n-1}, \hat{Z}_h^n) \right) = \partial_{\hat{U}} \mathcal{J}(q, \hat{U})(\hat{\Psi}) \quad \forall (\hat{\Psi}_h^n)_{n=1}^N \in \hat{X}_h^N. \end{aligned} \quad (16)$$

Here, $\partial_{\hat{U}_h^n} \hat{A}$ denotes the directional derivative of the form \hat{A} with respect to its \hat{U}^n argument, and the first argument of the second parentheses denotes the respective direction.

With this adjoint, we obtain the total derivative of the cost functional $q \mapsto \mathcal{J}(q) := \mathcal{J}(q, \hat{U})$ in a direction δq as

$$\frac{d}{dq} \mathcal{J}(q, \hat{U}) \delta q = \partial_q \mathcal{J}(q, \hat{U})(\delta q) + \sum_{n=1}^N \left(\theta k \partial_q \hat{A}_E(q, \hat{U}_h^n)(\delta q, \hat{Z}_h^n) + (1 - \theta) k \partial_q \hat{A}_E(q, \hat{U}_h^{n-1})(\delta q, \hat{Z}_h^n) \right)$$

allowing the calculation of the reduced gradient $\nabla J(q) \in \mathbb{R}^p$ of the cost functional by

$$(\nabla J(q), \delta q) = \frac{d}{dq} \mathcal{J}(q, \hat{U}) \delta q \quad \forall \delta q \in \mathbb{R}^p \quad (17)$$

cf., for example, Reference 47.

5 | SOLUTION ALGORITHMS

In order to minimize the cost functional $\mathcal{J}(q)$, we consider two solution algorithms in this work. First, we employ a standard globalized gradient method. Second, as it is well known that gradient methods suffer from bad-scaling in the problem, we additionally design an inverse Broyden-Fletcher-Goldfarb-Shanno (BFGS, for example, Reference 66) method.

The gradient method reads:

Algorithm 1 . Gradient method

Let $q^0 \in \mathbb{R}^p$ be an initial guess, and pick parameters $\gamma \in (0, 1/2)$ and $\beta \in (0, 1)$. For $k = 0, 1, \dots$ until $\|\nabla_q \mathcal{J}(q^k)\|_Q < TOL$ iterate

1. Solve the (nonlinear) primal problem (15) to obtain $\hat{U}_h \in \hat{X}_h^N$ using Algorithm 3.
2. Solve the (linear) adjoint problem (16) to obtain $\hat{Z}_h \in \hat{X}_h^N$.
3. Compute the gradient $\nabla \mathcal{J}(q^k)$ using (17).
4. Find the largest $l \in \{0, 1, \dots\}$ such that (Armijo-rule)

$$\mathcal{J}(q^k - \beta^l \nabla \mathcal{J}(q^k)) \leq \mathcal{J}(q^k) - \gamma \beta^l \|\nabla \mathcal{J}(q^k)\|^2$$

holds and set $\beta_k = \beta^l$.

5. Update

$$q^{k+1} = q^k - \beta_k \nabla \mathcal{J}(q^k).$$

The BFGS method is defined as:

Algorithm 2 . Inverse BFGS method

Let $q^0 \in \mathbb{R}^p$ and $B_0 \in \mathbb{R}^{p \times p}$ be an initial guess for the control and inverse Hessian, and pick parameters $\gamma \in (0, 1/2)$ and $\eta \in (\gamma, 1)$. For $k = 0, 1, \dots$ until $\|\nabla_q \mathcal{J}(q^k)\|_Q < TOL$ iterate

1. Solve the (nonlinear) primal problem (15) to obtain $\hat{U}_h \in \hat{X}_h^N$ using Algorithm 3.
2. Solve the (linear) adjoint problem (16) to obtain $\hat{Z}_h \in \hat{X}_h^N$.
3. Compute the gradient $\nabla \mathcal{J}(q^k)$ using (17) and set $d^k = -B_k \nabla \mathcal{J}(q^k)$.
4. Find a step-length t_k such that the Powell-Wolfe conditions

$$\begin{aligned} \mathcal{J}(q^k - t_k d^k) &\leq \mathcal{J}(q^k) + \gamma t_k \langle \nabla \mathcal{J}(q^k), d^k \rangle, \\ \langle \nabla \mathcal{J}(q^k + t_k d^k), d^k \rangle &\geq \eta \langle \nabla \mathcal{J}(q^k), d^k \rangle \end{aligned}$$

hold.

5. Set $y^k = \nabla \mathcal{J}(q^k + t_k d^k) - \nabla \mathcal{J}(q^k)$, and update

$$B_{k+1} = B_k + \frac{(t_k d^k - B_k y^k)(d^k)^T + t_k d^k (d^k - B_k y^k)^T}{\langle d^k, y^k \rangle} - \frac{\langle t_k d^k - B_k y^k, y^k \rangle}{\langle d^k, y^k \rangle^2} d^k (d^k)^T$$

6. Update

$$q^{k+1} = q^k + t_k d^k.$$

Remark 2. Since it is easy to guess and invert the Hessian part corresponding to $\alpha \|q\|^2$, we always utilize $B_0 = \frac{1}{\alpha} I \in \mathbb{R}^{p \times p}$. To obtain a step-length satisfying the Powell-Wolfe conditions we utilize [67, algorithm 9.3].

In both optimization algorithms, the nonlinear FSI forward problem (15) needs to be solved. At each time point the following problem is given:

$$\hat{A}(\hat{U}_h^n)(\hat{\Psi}) = 0 \quad \forall \hat{\Psi} \in \hat{X}_h.$$

To this end, we employ the following classical algorithm:

Algorithm 3 . Residual-based Newton's method for solving the forward problem

We omit h and n for the convenience of the reader. Choose an initial Newton guess $\hat{U}^0 \in \hat{X}$. For the iteration steps $k = 0, 1, 2, 3, \dots$:

6.2 | Example 1: Optimal design within the FSI 1 benchmark

In this first numerical example, we consider a quasistationary setting based on the FSI 1 benchmark.^{4,16} The forward problem is solved with the BE scheme, that is, $\theta = 1$, since the configuration is stationary and we only use a time-dependent method to find the stationary limit.

Formulation 9. The optimization problem reads: design of the Lamé parameter $q := \mu_s$ from desired displacements of the beam-tip at $A := (0.6, 0.2)$ by minimizing the cost functional (21). The exact values u_d are taken from a reference solution with $\mu = 0.5 \cdot 10^6 \text{ kg/ms}^2$.

6.2.1 | Cost functional

The cost functional reads:

$$J(q, \hat{U}) = \frac{1}{2}(\hat{u}_1(A, T) - u_d)^2 + \frac{\alpha}{2}|q - q_d|^2, \quad (21)$$

with $u_d = 2.27007 \cdot 10^{-5}$ and q_d will be specified in the respective computations.

6.2.2 | Configuration

The geometry of the FSI-1 and FSI-3 settings are displayed in Figure 1. An elastic beam is attached to a cylinder and is surrounded by an incompressible fluid. The initial geometry is once uniformly refined in space.

On the cylinder and outer boundary Γ_w we enforce zero Dirichlet boundary conditions for \hat{v} and \hat{u} . On the outflow boundary Γ_{out} we prescribe the do-nothing outflow condition.⁷¹ The inflow profile on Γ_{in} is given by:

$$\hat{v}(0, y) := 1.5 y (0.41 - y) \frac{4}{0.41^2} v_{\text{mean}}(t).$$

The mean inflow $v_{\text{mean}}(t)$ is 0.2 m/s for Example 1 (FSI 1) and 2.0 m/s in Example 2 (FSI 3). In the FSI 1 test case, we compute $n = 25$ time steps using $k = 1 \text{ s}$ and in the FSI 3 example, we work with $k = 0.001 \text{ s}$ with $T = 0.6 \text{ s}$ corresponding to $n = 6000$ time steps.

6.2.3 | Discussion of the FSI 1 findings

Our results for three different configurations are displayed in the Tables 2, 3, and 4. In the first run with $\alpha = 0.001$, the algorithm converges slowly in order to estimate q^k and to reduce the cost functional $\mathcal{J}(q^k)$. The main reason is due to the low regularization, which is confirmed by two further runs with $\alpha = 0.1$ and 1 . In the first two tests, Tables 2 and 3, the reduction in the computational cost between the gradient-based algorithm and the BFGS method is significant. In the

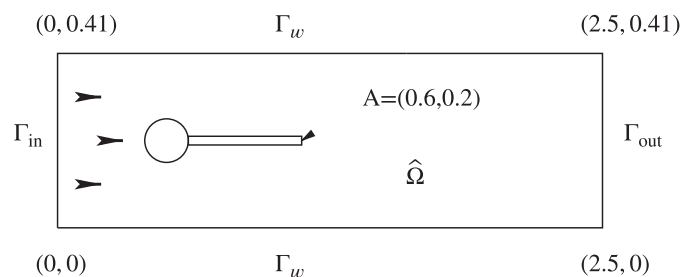


FIGURE 1 FSI-1 and FSI-3 benchmarks (Examples 1 and 2): flow around cylinder with elastic beam with circle-center $C = (0.2, 0.2)$ and radius $r = 0.05$. FSI, fluid-structure interaction

last test, Table 4, the difference reduces. Due to the higher cost in steps four and five of the BFGS algorithm, the overall performance of both algorithms is similar.

In Table 3, the value of α is enlarged to 0.1. Here, in 155 gradient iterations, the cost functional is reduced by an order to 10^{14} from an initial control $q^0 = 5000$ to $q^{155} = 10^6$.

Increasing further α to 1 (Table 3) yields a reduction in $\mathcal{J}(q^k)$ from about 10^{11} to 10^{-6} . The gradient algorithm converges in five iterations.

6.3 | Example 2: Optimal design within the FSI 3 benchmark

In this second numerical test, we employ the same geometry as in Example 1. The material parameters and boundary data can be found in Table 1 and Section 6.2.2. Since this numerical test is nonstationary with periodic solutions in the original forward run, we use the shifted Crank-Nicolson time-stepping scheme with minimal numerical dissipation.

Formulation 10. We consider an optimal design problem for $q := \mu_s$ such that the displacement value at the beam-tip at (0.6, 0.4) is close to a desired displacement u_d obtained by the FSI 1 simulation in Example 1, but not FSI 3. To this end, (22) is minimized.

6.3.1 | Cost functional

The cost functional is given by:

$$J(q, \hat{U}) = \frac{1}{2}(\hat{u}_1(A, T) - u_d)^2 + \frac{\alpha}{2}|q - q_d|^2 \quad (22)$$

with $u_d = 2.27007 \cdot 10^{-5}$ and q_d will be specified in the respective computations.

6.3.2 | Discussion of the FSI 3 findings

Graphical plots of the solution are provided in Figure 2. Our quantitative results are shown in Table 5. The gradient algorithm converges in 29 iterations in which the cost functional is reduced by 10^3 and the control is approximated by $q^{29} = 572\,378$.

Similar to Example 1, the reduction in the computational cost between the gradient-based algorithm and the BFGS method is significant as being observed in Table 5.

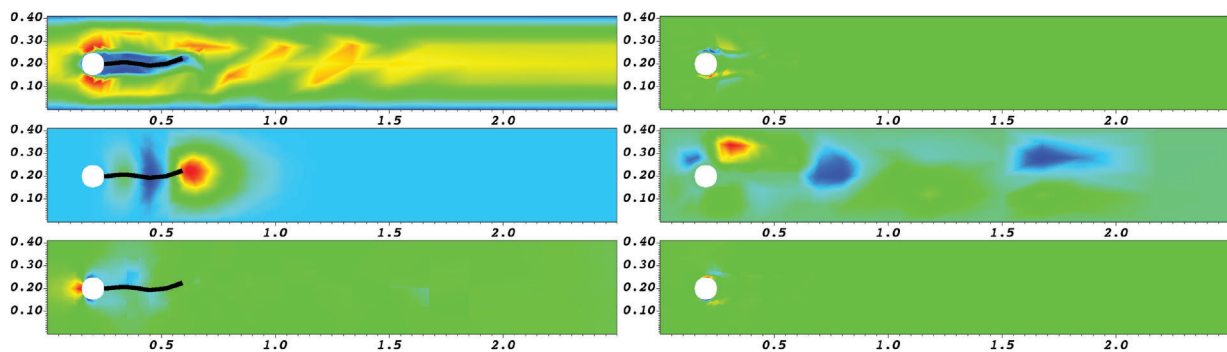


FIGURE 2 Example 2: At $T = 5s$ (time step No. 5000): $v_x(t)$, $u_y(t)$, and $p(t)$ in the deformed configuration $\Omega(t)$. Left column: the primal states are shown. Right column: the corresponding adjoint states are shown

TABLE 2 Optimization results for the FSI 1 example with $\alpha = 0.001$ and $q_d = 10^6$

Iter	Gradient method			BFGS method		
	$J(q^k)$	q^k	$\frac{ \nabla J(q^k) }{ \nabla J(q^0) }$	$J(q^k)$	q^k	$\frac{ \nabla J(q^k) }{ \nabla J(q^0) }$
0	$4.913 \cdot 10^8$	5000	$1.0000 \cdot 10^{-0}$	$4.913 \cdot 10^8$	5000	$1.0000 \cdot 10^{-0}$
1	$4.9033 \cdot 10^8$	5987.54	$9.9901 \cdot 10^{-1}$	$2.758 \cdot 10^4$	99 2545	$7.4929 \cdot 10^{-3}$
2	$4.8936 \cdot 10^8$	6974.11	$9.9802 \cdot 10^{-1}$	$6.361 \cdot 10^{-11}$	10^6	$< 10^{-11}$
3	$4.8838 \cdot 10^8$	7959.69	$9.9703 \cdot 10^{-1}$			
⋮	⋮	⋮	⋮			
101	$4.0201 \cdot 10^8$	99 950.5	$9.0457 \cdot 10^{-1}$			
102	$4.0121 \cdot 10^8$	100844	$9.0367 \cdot 10^{-1}$			
103	$4.0042 \cdot 10^8$	101736	$9.0278 \cdot 10^{-1}$			
⋮	⋮	⋮	⋮			
198	$3.3157 \cdot 10^8$	182600	$8.2151 \cdot 10^{-1}$			
199	$3.3091 \cdot 10^8$	183411	$8.2069 \cdot 10^{-1}$			
200	$3.3025 \cdot 10^8$	184222	$8.1988 \cdot 10^{-1}$			
⋮	⋮	⋮	⋮			

Note: The initial Residual in $q_0 = 5000$ is $|\nabla J(q^0)| = 987.5$.

Abbreviations: BFGS, Broyden-Fletcher-Goldfarb-Shanno; FSI, fluid-structure interaction.

TABLE 3 Optimization results for the FSI 1 example with $\alpha = 0.1$ and $q_d = 10^6$

Iter	Gradient method			BFGS method		
	$J(q^k)$	q^k	$\frac{ \nabla J(q^k) }{ \nabla J(q^0) }$	$J(q^k)$	q^k	$\frac{ \nabla J(q^k) }{ \nabla J(q^0) }$
0	$4.913 \cdot 10^{10}$	5000	$1.0000 \cdot 10^{-0}$	$4.913 \cdot 10^{10}$	5000	$1.0000 \cdot 10^{-0}$
1	$3.9862 \cdot 10^{10}$	103754	$9.0075 \cdot 10^{-1}$	$2.758 \cdot 10^6$	992 545	$7.4929 \cdot 10^{-3}$
2	$3.2342 \cdot 10^{10}$	192707	$8.1135 \cdot 10^{-1}$	$6.360 \cdot 10^{-11}$	10^6	$< 10^{-11}$
3	$2.6241 \cdot 10^{10}$	272832	$7.3082 \cdot 10^{-1}$			
⋮	⋮	⋮	⋮			
101	$3.3216 \cdot 10^1$	999974	$2.6001 \cdot 10^{-5}$			
102	$2.6950 \cdot 10^1$	999977	$2.3421 \cdot 10^{-5}$			
103	$2.1865 \cdot 10^1$	999979	$2.1096 \cdot 10^{-5}$			
⋮	⋮	⋮	⋮			
154	$5.1211 \cdot 10^{-4}$	10^6	$1.0210 \cdot 10^{-7}$			
155	$4.1550 \cdot 10^{-4}$	10^6	$9.1962 \cdot 10^{-8}$			

Note: The initial Residual in $q_0 = 5000$ is $|\nabla J(q^0)| = 9.875 \cdot 10^4$.

Abbreviations: BFGS, Broyden-Fletcher-Goldfarb-Shanno; FSI, fluid-structure interaction.

TABLE 4 Optimization results for the FSI 1 example with $\alpha = 1$ and $q_d = 500\,000$

Iter	Gradient method			BFGS method		
	$J(q^k)$	q^k	$\frac{ \nabla J(q^k) }{ \nabla J(q^0) }$	$J(q^k)$	q^k	$\frac{ \nabla J(q^k) }{ \nabla J(q^0) }$
0	$1.216 \cdot 10^{11}$	5000	$1.0000 \cdot 10^{-0}$	$1.216 \cdot 10^{11}$	5000	$1.0000 \cdot 10^{-0}$
1	$6.8268 \cdot 10^6$	496291	$7.4929 \cdot 10^{-3}$	$6.827 \cdot 10^6$	496 291	$7.4929 \cdot 10^{-3}$
2	$3.8328 \cdot 10^2$	499972	$5.6144 \cdot 10^{-5}$	$1.187 \cdot 10^{-17}$	500 000	$< 10^{-11}$
3	$2.1519 \cdot 10^{-2}$	500000	$4.2068 \cdot 10^{-7}$			
4	$1.2082 \cdot 10^{-6}$	500000	$3.1522 \cdot 10^{-9}$			

Note: The initial Residual in $q_0 = 5000$ is $|\nabla J(q^0)| = 4.913 \cdot 10^5$.

Abbreviations: BFGS, Broyden-Fletcher-Goldfarb-Shanno; FSI, fluid-structure interaction.

TABLE 5 Optimization results for the FSI-3 example with $\alpha = 0.1$ and $q_d = 500\,000$

Iter	Gradient method			BFGS method		
	$J(q^k)$	q^k	Residual	$J(q^k)$	q^k	Residual
0	$1.117 \cdot 10^{11}$	$2 \cdot 10^6$	$1.0000 \cdot 10^{-0}$	$1.117 \cdot 10^{11}$	$2 \cdot 10^6$	$1.0000 \cdot 10^{-0}$
1	$9.0593 \cdot 10^{10}$	$1.85112 \cdot 10^6$	$9.0075 \cdot 10^{-1}$	$6.270 \cdot 10^6$	511 239	$7.4929 \cdot 10^{-3}$
2	$7.3502 \cdot 10^{10}$	$1.71702 \cdot 10^6$	$8.1135 \cdot 10^{-1}$	$1.653 \cdot 10^{-6}$	500 000	$< 10^{-11}$
3	$5.9636 \cdot 10^{10}$	$1.59623 \cdot 10^6$	$7.3082 \cdot 10^{-1}$			
	\vdots	\vdots	\vdots			
100	$7.5488 \cdot 10^1$	500043	$2.8866 \cdot 10^{-5}$			
101	$6.1247 \cdot 10^1$	500039	$2.6001 \cdot 10^{-5}$			
	\vdots	\vdots	\vdots			
154	$9.4595 \cdot 10^{-4}$	500000	$1.0210 \cdot 10^{-7}$			
155	$9.4595 \cdot 10^{-4}$	500000	$9.1962 \cdot 10^{-8}$			

Note: The initial Residual in $q_0 = 2 \cdot 10^6$ is $1.489 \cdot 10^5$.

Abbreviations: BFGS, Broyden-Fletcher-Goldfarb-Shanno; FSI, fluid-structure interaction.

6.4 | Example 3: 2D flapping membranes

In this third example, we consider 2D flap dynamics. This test is a challenge because of the thin flaps and the mesh regularity. The original setups for forward simulations were inspired by Reference 50. Our configuration here is a further extension, toward FSI-optimization, of References 51 and 21.

The problem statement reads:

Formulation 11. Design of the Lamé parameter $q := \mu_s$ in the elastic flaps such that the wall stresses are minimized. To this end, we consider the cost functional (23) to be minimized.

6.4.1 | Cost functional

The cost functional is given by:

$$J(q, \hat{U}) = F(\hat{\Gamma}_{\text{opt}}, T) + \frac{\alpha}{2} |q - q_d|^2 \quad (23)$$

where $q_d = 10^6$, and T is the end time value as in the other examples and $F(\cdot)$ is the wall stress functional in e_1 direction (here x -direction) defined as

$$F(\hat{\Gamma}_{\text{opt}}, T) := \int_{\hat{\Gamma}_{\text{opt}}} (\hat{\sigma}_f \cdot \hat{n}) \cdot e_1 \, ds \quad (24)$$

where \hat{n} is the unit normal vector pointing outward of the domain $\hat{\Omega}_s$ and e_1 the first unit vector in \mathbb{R}^2 . The boundary part, where the drag is evaluated is

$$\hat{\Gamma}_{\text{opt}} := \{2 \leq x \leq 8; y = 0\}.$$

Moreover, we notice that we only control μ in the elastic flaps, while in the rest of the solid, the value is as in Table 1.

FIGURE 3 Example 3: Configuration. All data given in cm

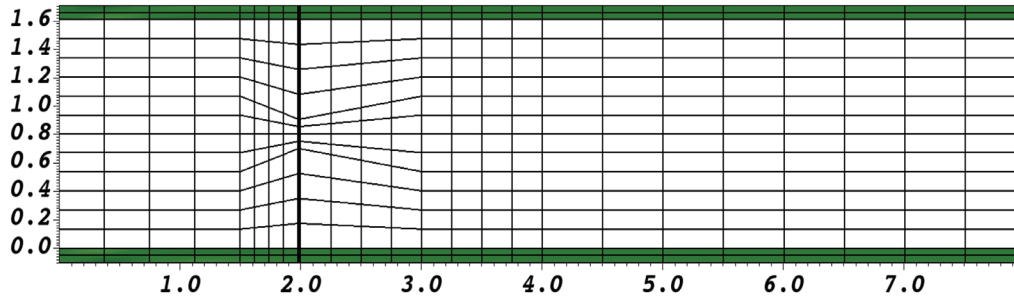
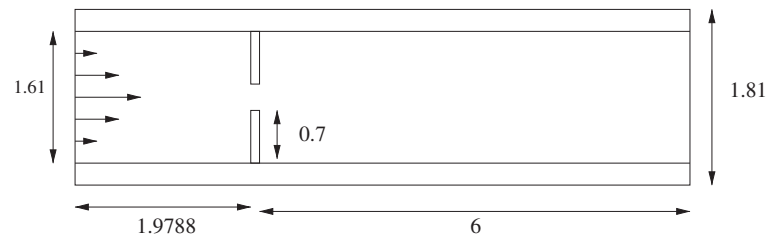
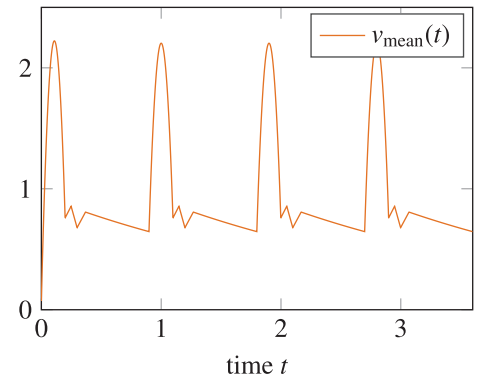


FIGURE 4 The mesh for the flapping membranes example at the initial time step. All geometric values are given in cm. The solid boundaries are colored in dark green. The flaps are located at $1.9788 \text{ cm} \leq x \leq 2.0 \text{ cm}$

FIGURE 5 Interpolated flow rate profile $\bar{v}(t)$ that is used to scale the inflow profile of the flapping membrane example



6.4.2 | Configuration

The geometry is shown in Figure 3. The initial mesh is once uniformly refined yielding the mesh shown in Figure 4.

On the inflow boundary, $\hat{\Gamma}_{\text{in}} := \{x = 0; -0.1 \leq y \leq 1.61\}$, we prescribe a parabolic inflow profile

$$v(0, y) := 0.15y(1.61 - y) \frac{4}{1.61^2} v_{\text{mean}}(t) \quad \text{for } t \in I := [0, 0.9],$$

where $v_{\text{mean}}(t)$ taken from Figure 5.

At the outflow boundary the do-nothing outflow condition $\hat{\Gamma}_{\text{out}}$ is prescribed for \hat{v} and \hat{p} , while the displacements are fixed there. On the outer wall boundaries

$$\hat{\Gamma}_{\text{wall}} := \{0 \leq x \leq 8; y = -0.1\} \cup \{0 \leq x \leq 8; y = -1.61\}$$

we use homogeneous Neumann conditions for the displacements and the velocity in order to allow the solid to move freely.

The computations are performed on the time interval $I = (0, 0.579375 \text{ s})$. The end time value $T = 0.579375 \text{ s}$ is chosen such that the first maximal stress appears for the initial control q^0 . For the computations, the time interval is split into 618 time steps.

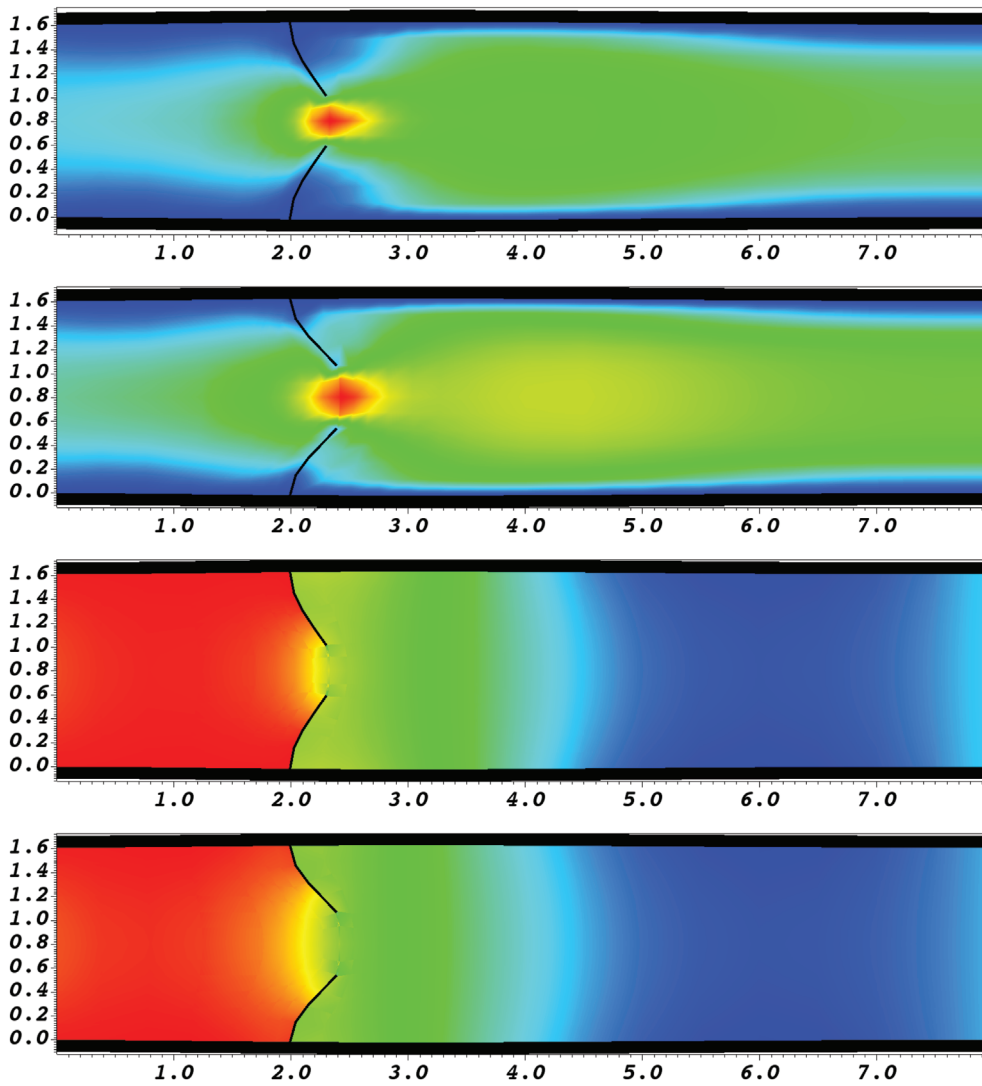


FIGURE 6 Example 3: At $T = 0.579375$ s (time step No. 618): $v_x(t)$ and $p(t)$ are displayed in the deformed configuration $\Omega(t)$. Going from top to bottom: $v_x(t = 0.579375$ s) in the optimization cycle 0 (classical forward run with $\mu = q^0 = 2 \cdot 10^7$). The maximum velocity (in red) has the value 3.15 cm/s. In the second row, $v_x(t = 0.579375$ s) in the eighth optimization cycle is displayed; here $\mu = q^8 = 5 \cdot 10^6$, which means less-stiff flaps and corresponding higher displacements. Consequently, the maximum velocity is reduced and has the value 2.3 cm/s. In the rows three and four the corresponding pressure fields are shown. The maximum pressure values are 3012 and 2825 g/cm², respectively

6.4.3 | Discussion of the flapping membrane findings

The flow and pressure fields in the physical configuration $\Omega(t)$ are displayed in Figure 6. Therein, it is visible that the solid flaps undergo large deformations. In the optimized configuration after eight cycles the flaps even deform more. Here, a robust mesh motion model is indispensable. In Table 6, the performance of the optimization procedure is shown. A reduction of 10^{12} in the cost functional is achieved. The optimal q^8 is $5 \cdot 10^6$.

Furthermore, we observe that the reduction in the computational cost between the gradient-based algorithm and the BFGS method is less significant in this example as shown in Table 6.

7 | CONCLUSIONS

In this work, we developed settings for FSI-based optimization. Therein, the FSI problem is nonlinear and nonstationary and allows for large solid deformations. Consequently, when working with the ALE technique, a robust mesh motion model must be chosen. Here, it is based on a biharmonic equation. Based on this forward model, we provide the adjoint state, which is running backward-in-time. The resulting FSI-optimization problems are solved with a gradient-type and an inverse BFGS method. Three numerical examples are designed to investigate the performance of our algorithmic techniques. In the first numerical test an extension of the steady-state FSI 1 benchmark is considered. In the second and third examples, fully nonstationary tests are investigated. Specifically, the last numerical test is numerically challenging, even for the forward problem, because the flaps are very thin, while undergoing large solid deformations. Here, we observe significant reductions of the cost functional and excellent convergence properties of the optimization

TABLE 6 Optimization results for the flapping membrane example with $\alpha = 1$ and $q_d = 5 \cdot 10^6$

Iter	Gradient method			BFGS method		
	$J(q^k)$	q^k	$\frac{ \nabla J(q^k) }{ \nabla J(q^0) }$	$J(q^k)$	q^k	$\frac{ \nabla J(q^k) }{ \nabla J(q^0) }$
0	$1.265 \cdot 10^{14}$	$2 \cdot 10^7$	$1.0000 \cdot 10^{-0}$	$1.265 \cdot 10^{14}$	$2 \cdot 10^7$	$1.0000 \cdot 10^{-0}$
1	$1.9517 \cdot 10^{12}$	$3.13665 \cdot 10^6$	$1.2422 \cdot 10^{-1}$	$1.952 \cdot 10^{12}$	$3.13665 \cdot 10^6$	$1.242 \cdot 10^{-1}$
2	$3.0118 \cdot 10^{10}$	$5.23147 \cdot 10^6$	$1.5432 \cdot 10^{-2}$	$8.346 \cdot 10^2$	$5 \cdot 10^6$	$< 10^{-11}$
3	$4.6476 \cdot 10^8$	$4.97125 \cdot 10^6$	$1.9170 \cdot 10^{-3}$			
4	$7.1728 \cdot 10^6$	$5.00357 \cdot 10^6$	$2.3813 \cdot 10^{-4}$			
5	$1.1151 \cdot 10^5$	$4.99956 \cdot 10^6$	$2.9582 \cdot 10^{-5}$			
6	$2.5424 \cdot 10^3$	$5.00006 \cdot 10^6$	$3.6747 \cdot 10^{-6}$			
7	$8.6090 \cdot 10^2$	$4.99999 \cdot 10^6$	$4.5649 \cdot 10^{-7}$			
8	$8.3495 \cdot 10^2$	$5 \cdot 10^6$	$5.6707 \cdot 10^{-8}$			

Note: The initial Residual in $q_0 = 2 \cdot 10^7$ is $|\nabla J(q^0)| = 1.686 \cdot 10^7$.

Abbreviations: BFGS, Broyden-Fletcher-Goldfarb-Shanno; FSI, fluid-structure interaction.

algorithm. Furthermore, the BFGS algorithm yields a significant reduction in the computational cost compared with a gradient-based approach for the first two numerical examples. In the flapping membrane test, still the BFGS has fewer iterations, however, the higher cost in constructing the algorithm should be kept in mind here.

ACKNOWLEDGEMENT

Open access funding enabled and organized by Projekt DEAL.

ORCID

Thomas Wick  <https://orcid.org/0000-0002-6571-8043>

REFERENCES

- Bungartz HJ, Schäfer M. *Fluid-Structure Interaction: Modelling, Simulation, Optimization*. 53 of *Lecture Notes in Computational Science and Engineering*. New York, NY: Springer; 2006.
- Formaggia L, Quarteroni A, Veneziani A. *Cardiovascular Mathematics: Modeling and Simulation of the Circulatory System*. Italia, Milano: Springer-Verlag; 2009.
- Galdi G, Rannacher R. *Fundamental Trends in Fluid-Structure Interaction*. Singapore: World Scientific; 2010.
- Bungartz HJ, Mehl M, Schäfer M. *Fluid-Structure Interaction II: Modelling, Simulation, Optimization*. *Lecture Notes in Computational Science and Engineering*. New York, NY: Springer; 2010.
- Bazilevs Y, Takizawa K, Tezduyar T. *Computational Fluid-Structure Interaction: Methods and Applications*. Hoboken, NJ: Wiley; 2013.
- Bodnár T, Galdi G, Nečasová Š. *Fluid-Structure Interaction and Biomedical Applications*. *Advances in Mathematical Fluid Mechanics*. Basel, Switzerland: Springer; 2014.
- Richter T. *Fluid-Structure Interactions: Models, Analysis, and Finite Elements*. New York, NY: Springer; 2017.
- Frei S, Holm B, Richter T, Wick T, Yang H. *Fluid-structure interactions: Fluid-structure interaction modeling, adaptive discretisations and Solvers de Gruyter*; 2017.
- Causin P, Gerbeau JF, Nobile F. Added-mass effect in the design of partitioned algorithms for fluid-structure problems. *Comput Methods Appl Mech Eng*. 2005;194:4506-4527.
- Förster C, Wall WA, Ramm E. Artificial added mass instabilities in sequential staggered coupling of nonlinear structures and incompressible viscous flows. *Comput Methods Appl Mech Eng*. 2007;196(7):1278-1293. <https://doi.org/10.1016/j.cma.2006.09.002>.
- Asterino M, Chouly F, Fernández F. An added-mass free semi-implicit coupling scheme for fluid-structure interaction. *C R Acad Sci Paris Sér I*. 2009;347(1-2):99-104.
- Brummelen EHV. Added mass effects of compressible and incompressible flows in fluid-structure interaction. *ASME J Appl Mech*. 2009;76(2):021206.
- Donéa J, Fasoli-Stella P, Giuliani S. Lagrangian and Eulerian finite element techniques for transient fluid-structure interaction problems; 1977:Paper B1/2.
- Hughes T, Liu W, Zimmermann T. Lagrangian-Eulerian finite element formulation for incompressible viscous flows. *Comput Methods Appl Mech Eng*. 1981;29:329-349.
- Formaggia L, Nobile F. A stability analysis for the arbitrary Lagrangian Eulerian formulation with finite elements. *East-West J Numer Math*. 1999;7:105-132.

16. Hron J, Turek S. *Proposal for numerical benchmarking of fluid-structure interaction between an elastic object and laminar incompressible flow*. Vol 53. New York, NY: Springer-Verlag; 2006:146-170.
17. Dunne T, Richter T, Rannacher R. *Numerical Simulation of Fluid-Structure Interaction Based on Monolithic Variational Formulations*. Contemporary Challenges in Mathematical Fluid Mechanics. World Scientific, Singapore: Springer; 2010:1-75.
18. Goll C, Wick T, Wollner W. DOpElib: differential equations and optimization environment; a goal oriented software library for solving PDEs and optimization problems with PDEs. *Arch Numer Softw*. 2017;5(2):1-14. <https://doi.org/10.11588/ans.2017.2.11815>.
19. Wick T. Fluid-structure interactions using different mesh motion techniques. *Comput Struct*. 2011;89(13-14):1456-1467.
20. Wick T. Solving monolithic fluid-structure interaction problems in arbitrary Lagrangian Eulerian coordinates with the deal.II library. *Arch Numer Softw*. 2013;1:1-19.
21. Failer L, Wick T. Adaptive time-step control for nonlinear fluid-structure interaction. *J Comput Phys*. 2018;366:448-477.
22. Jodlbauer D, Langer U, Wick T. Parallel block-preconditioned monolithic solvers for fluid-structure interaction problems. *Int J Numer Methods Eng*. 2019;117(6):623-643.
23. Wick T, Wollner W. On the differentiability of fluid-structure interaction problems with respect to the problem data. *J Math Fluid Mech*. 2019;21(3). <https://doi.org/10.1007/s00021-019-0439-0>.
24. Lions JL. *Optimal Control of Systems Governed by Partial Differential Equations*. Die Grundlehren der mathematischen Wissenschaften. 1st ed. Berlin, Heidelberg/Germany, New York, NY: Springer; 1971.
25. Richter T, Wick T. Optimal control and parameter estimation for stationary fluid-structure interaction. *SIAM J Sci Comput*. 2013;35(5):B1085-B1104.
26. Wick T. Adaptive Finite Element Simulation of Fluid-Structure Interaction with Application to Heart-Valve Dynamics (PhD thesis). University of Heidelberg, Im Neuenheimer Feld 293/294; 2011.
27. Chirco L, Da Vià R, Manservigi S. An optimal control method for fluid structure interaction systems via adjoint boundary pressure. *J Phys Conf Ser*. 2017;923:012026. <https://doi.org/10.1088/1742-6596/923/1/012026>.
28. Zee K, Brummelen E, Akkerman I, Borst R. Goal-oriented error estimation and adaptivity for fluid-structure interaction using exact linearized adjoints. *Comput Methods Appl Mech Eng*. 2011;200:2738-2757.
29. Richter T. Goal-oriented error estimation for fluid-structure interaction problems. *Comput Methods Appl Mech Eng*. 2012;223-224:28-42.
30. Singhammer K. Optimal control of stationary fluid-structure interaction with partitioned methods (PhD thesis). Technische Universität München, Boltzmannstr. Vol. 3; 2019.
31. Moubachir M, Zolésio JP. Optimal control of fluid-structure interaction systems: the case of a rigid solid. Research Report RR-4611, INRIA; 2002.
32. Bucci F, Lasiecka I. Optimal boundary control with critical penalization for a PDE model of fluid-solid interactions. *Calc Var*. 2010;37(1-2):217-235. <https://doi.org/10.1007/s00526-009-0259-9>.
33. Perego M, Veneziani A, Vergara C. A variational approach for estimating the compliance of the cardiovascular tissue: an inverse fluid-structure interaction problem. *SIAM J Sci Comput*. 2011;33(3):1181-1211.
34. Guerra T, Tiago J, Sequeira A. Optimal control in blood flow simulations. *Int J Non-Linear Mech*. 2014;64:57-69. <https://doi.org/10.1016/j.ijnonlinmec.2014.04.005>.
35. D'Elia M, Mirabella L, Passerini T, et al. *Applications of Variational Data Assimilation in Computational Hemodynamics*. Milan, Italy: Springer; 2012:363-394.
36. Bertoglio C, Moireau P, Gerbeau J. Sequential parameter estimation in fluid-structure problems. Application to hemodynamics. *Int J Numer Meth Biomed Des Eng*. 2012;28:434-455. <https://doi.org/10.1002/cnm.1476>.
37. Poireau P, Bertoglio C, Xiao N, et al. Sequential identification of boundary support parameters in a fluid-structure vascular model using patient image data. *Biomech Model Mechanobiol*. 2013;12(3):475-496.
38. Bertoglio C, Barber D, Gaddum N, et al. Identification of artery wall stiffness: in vitro validation and in vivo results of a data assimilation procedure applied to a 3D fluid-structure interaction model. *J Biomech*. 2014;47(5):1027-1034.
39. Kuberry P, Lee H. A decoupling algorithm for fluid-structure interaction problems based on optimization. *Comput Methods Appl Mech Eng*. 2013;267:594-605. <https://doi.org/10.1016/j.cma.2013.10.006>.
40. Degroote J, Hojjat M, Stavropoulou E, Wüchner R, Bletzinger KU. Partitioned solution of an unsteady adjoint for strongly coupled fluid-structure interactions and application to parameter identification of a one-dimensional problem. *Struct Multidiscip Optim*. 2013;47(1):77-94. <https://doi.org/10.1007/s00158-012-0808-2>.
41. Martin V, Clément F, Decoene A, Gerbeau JF. Parameter identification for a one-dimensional blood flow model. *ESAIM Proc*. 2005;14:174-200. <https://doi.org/10.1051/proc:2005014>.
42. Lassila T, Manzoni A, Quarteroni A, Rozza G. A reduced computational and geometrical framework for inverse problems in hemodynamics. *Int J Numer Meth Biomed Eng*. 2013;29(7):741-776. <https://doi.org/10.1002/cnm.2559>.
43. Bazilevs Y, Hsu MC, Bement M. Adjoint-based control of fluid-structure interaction for computational steering applications. *Proc Comput Sci*. 2013;18:1989-1998. <https://doi.org/10.1016/j.procs.2013.05.368>.
44. Failer L, Meidner D, Vexler B. Optimal control of a linear unsteady fluid-structure interaction problem. *J Optim Theory Appl*. 2016;170(1):1-27. <https://doi.org/10.1007/s10957-016-0930-1>.
45. Failer L. Optimal Control of Time-Dependent Nonlinear Fluid-Structure Interaction (PhD thesis). Technische Universität München, Boltzmannstr Vol. 3; 2017.
46. Kratzke J. Uncertainty Quantification for Fluid-Structure Interaction: Application to Aortic Biomechanics (PhD thesis). University of Heidelberg, Im Neuenheimer Feld 293/294; 2018.

47. Becker R, Meidner D, Vexler B. Efficient numerical solution of parabolic optimization problems by finite element methods. *Optim Methods Softw.* 2007;22(5):813-833. <https://doi.org/10.1080/10556780701228532>.
48. Allaire G. A review of adjoint methods for sensitivity analysis, uncertainty quantification and optimization in numerical codes. *Ingenieurs de l'Automobile, SIA, HAL Id: hal-01242950.* 2015;836:33-36.
49. Fischer M, Lindemann F, Ulbrich M, Ulbrich S. Frechet differentiability of unsteady incompressible Navier–stokes flow with respect to domain variations of low regularity by using a general analytical framework. *SIAM J Control Optim.* 2017;55(5):3226-3257.
50. Gil AJ, Carreno AA, Bonet J, Hassan O. The immersed structural potential method for haemodynamic applications. *J Comp Phys.* 2010;229:8613-8641.
51. Wick T. Flapping and contact FSI computations with the fluid-solid interface-tracking/interface-capturing technique and mesh adaptivity. *Comput Mech.* 2014;53(1):29-43.
52. Dautray R, Lions JL. *Mathematical Analysis and Numerical Methods for Science and Technology.* Vol 5. Springer-Verlag.: Berlin-Heidelberg/Germany; 2000.
53. Wloka J. *Partielle Differentialgleichungen.* Stuttgart, Germany: B. G. Teubner Verlag; 1982.
54. Evans LC. *Partial Differential Equations.* Vol 19. Rhode Island: American Mathematical Society; 2000.
55. Hron J, Turek S. *A Monolithic FEM/Multigrid Solver for ALE Formulation of Fluid structure with Application in Biomechanics.* New York, NY: Springer-Verlag; 2006:146-170.
56. Dunne T. Adaptive Finite Element Approximation of Fluid-Structure Interaction Based on Eulerian and Arbitrary Lagrangian-Eulerian Variational Formulations (PhD thesis). University of Heidelberg, Im Neuenheimer Feld 293/294; 2007.
57. Helenbrook B. Mesh deformation using the biharmonic operator. *Int J Numer Methods Eng.* 2003;56:1007-1021.
58. Holzapfel G. *Nonlinear Solid Mechanics: A Continuum Approach for Engineering.* Hoboken, NJ: John Wiley & Sons Ltd; 2000.
59. Rannacher R. On the stabilization of the Crank-Nicolson scheme for long time calculations; 1986.
60. Heywood JG, Rannacher R. Finite-element approximation of the nonstationary Navier-Stokes problem Part IV: error analysis for second-order time discretization. *SIAM J Numer Anal.* 1990;27(2):353-384.
61. Ciarlet PG. *The finite element method for elliptic problems.* Vol 2. Amsterdam, Netherlands: North-Holland; 1987.
62. Girault V, Raviart PA. *Finite Element Method for the Navier-Stokes Equations.* Computer Series in Computational Mathematics. New York, NY: Springer-Verlag; 1986.
63. Tröltzsch F. *Optimal control of partial differential equations. 112 of Graduate Studies in Mathematics.* Providence, RI: American Mathematical Society; 2010.
64. Hinze M, Pinnau R, Ulbrich M, Ulbrich S. *Optimization with PDE Constraints. 23 of Mathematical Modelling: Theory and Applications.* New York, NY: Springer; 2009.
65. Haubner J, Ulbrich M, Ulbrich S. Analysis of shape optimization problems for unsteady fluid-structure interaction. tech. rep., Technische Universität München; Boltzmannstr. Vol. 3:2019.
66. Nocedal J, Wright SJ. *Numerical Optimization.* New York, NY: Springer; 2006.
67. Ulbrich M, Ulbrich S. *Nichtlineare Optimierung.* Basel, Switzerland: Birkhäuser; 2012.
68. Davis TA, Duff IS. An unsymmetric-pattern multifrontal method for sparse LU factorization. *SIAM J Matrix Anal Appl.* 1997;18(1):140-158.
69. Dopleib. The differential equation and optimization environment: DOPELIB. <http://www.dopelib.net>.
70. Alzetta G, Arndt D, Bangerth W, et al. The deal.II library, version 9.0. *J Numer Math.* 2018;26(4):173-183. <https://doi.org/10.1515/jnma-2018-0054>.
71. Heywood JG, Rannacher R, Turek S. Artificial boundaries and flux and pressure conditions for the incompressible Navier-Stokes equations. *Int J Numer Methods Fluids.* 1996;22:325-352.

SUPPORTING INFORMATION

Additional supporting information may be found online in the Supporting Information section at the end of this article.

How to cite this article: Wick T, Wollner W. Optimization with nonstationary, nonlinear monolithic fluid-structure interaction. *Int J Numer Methods Eng.* 2021;122:5430–5449. <https://doi.org/10.1002/nme.6372>